Anisotropy-driven circular high-harmonic generation in semi-Dirac semimetals

Kartik Prabhu,[1] M. S. Mrudul,[2] and Gopal Dixit[1,3,4,*]

[1]*Department of Physics, Indian Institute of Technology Bombay, Powai, Mumbai 400076, India*
[2]*Department of Physics and Astronomy, Uppsala University, P.O. Box 516, SE-75120 Uppsala, Sweden*
[3]*SLAC National Accelerator Laboratory, Stanford PULSE Institute, 2575 Sand Hill Road, Menlo Park, California 94025, USA*
[4]*Max-Born Institute, Max-Born Straße 2A, D-12489 Berlin, Germany*

(Received 3 October 2025; revised 24 June 2026; accepted 24 July 2026; published 12 August 2026)

Generating elliptically polarized higher-order harmonics is essential for probing a wide range of chiral-sensitive light-matter interactions in nature. We demonstrate that semi-Dirac semimetals produce efficient odd-order harmonics under circularly polarized driving fields, remarkably contrasting with known two-dimensional semimetals, where circular polarization typically suppresses high-harmonic generation. The underlying mechanism is attributed to anisotropy-induced dipole coupling, which manifests distinctly in the ellipticity dependence of the harmonic yield. Specifically, the total yield is minimal for linear polarization and rises sharply as the polarization approaches circular, exhibiting nonmonotonic, harmonic-specific behavior. We find that the polarization dependence exhibits a pronounced twofold anisotropy, with each harmonic order showing a distinct angular distribution of maximum intensity. This characteristic anisotropy arises directly from the unique band dispersion of semi-Dirac semimetals. Our results not only uncover a link between anisotropic dispersion and strong-field nonlinear optics, but also position semi-Dirac semimetals as promising platforms for symmetry-engineered and polarization-tailored ultrafast light-matter control.

DOI: 10.1103/mxwy-m8zd

I. INTRODUCTION

Recent progress in intense laser technology has transformed our ability to interrogate quantum materials through their nonlinear optical responses [1–10]. In particular, the availability of intense midinfrared pulses has driven light-matter interactions beyond the perturbative regime, unveiling a plethora of nonperturbative phenomena. Among these, high-harmonic generation (HHG) is a hallmark strong-field process, enabling frequency up-conversion far beyond the perturbative limit and providing a pathway to attosecond pulse generation in the extreme-ultraviolet and soft x-ray regimes [11]. The first observation of nonperturbative HHG from zinc oxide marked an important milestone, extending HHG from gaseous media into the realm of solid-state systems [12]. Since its inception in 2011, solid-state HHG has emerged as the method of choice for unraveling numerous equilibrium and far-from-equilibrium properties of quantum materials, including subcycle electron dynamics [13–28]. Special emphasis has been placed on quantum semimetals, particularly Weyl and Dirac semimetals, as well as graphene, which is known to exhibit anomalous HHG responses [29–54].

The recent realization of semi-Dirac fermions in ZrSiS has introduced a compelling new member to the family of quantum semimetals [55]. These systems exhibit pronounced anisotropy in their low-energy excitations, with energy dispersion that is linear along one direction and quadratic along the orthogonal direction. This behavior stands in stark contrast to known Dirac materials, where the linear dispersion is isotropic with the band touching occurring at discrete points in momentum space. Interestingly, the semi-Dirac band structure can emerge from the merging of multiple Dirac points when the parent Dirac semimetals are tuned via external perturbations such as doping, strain, or pressure [56–61]. Moreover, the anisotropic energy dispersion in semi-Dirac semimetals differs fundamentally from that in multi-Weyl semimetals, where the anisotropic band-merging points are topologically protected [62,63]. Despite these advances, HHG in semi-Dirac semimetals remains unexplored territory. Understanding how such highly directional energy dispersions influence nonperturbative optical processes is therefore of fundamental importance, not only for uncovering the underlying light-matter interaction mechanisms, but also for paving the way toward ultrafast photonics and light-driven quantum technologies based on these systems. The present work focuses on exploring high-harmonic spectroscopy in semi-Dirac semimetals.

In this work, we demonstrate that the inherently anisotropic energy dispersion of semi-Dirac semimetals enables efficient HHG under circularly polarized driving field. The HHG efficiency for circular polarization exceeds that for linear polarization along a particular direction by several orders of magnitude. Furthermore, the harmonic yield exhibits a pronounced and highly orientation-sensitive dependence on the driving field's ellipticity, with the maximum yield occurring for circular or elliptical driving pulses. These behaviors

*Contact author: gdixit@phy.iitb.ac.in

Published by the American Physical Society under the terms of the Creative Commons Attribution 4.0 International license. Further distribution of this work must maintain attribution to the author(s) and the published article's title, journal citation, and DOI.

stand in sharp contrast to established results for pristine or strained graphene and nodal-line semimetals [33,42,64–66]. The emitted harmonics further display a pronounced anisotropy in their polarization dependence, providing a unique spectroscopic fingerprint of the semi-Dirac fermions and the underlying anisotropic band structure. Such control over both yield and polarization offers a powerful route for optimizing harmonic generation and tailoring the polarization properties of emitted light, capabilities that are particularly important for probing chiral-sensitive ultrafast light-matter interactions [67,68].

II. THEORY

To describe a two-dimensional semi-Dirac semimetal, we use a tight-binding Hamiltonian with a nearest-neighbor interaction as

$$\mathcal{H}(\mathbf{k}) = \begin{bmatrix} 0 & t_1 f^*(\mathbf{k}) \\ t_1 f(\mathbf{k}) & 0 \end{bmatrix}, \tag{1}$$

where $f(\mathbf{k}) = [e^{ik_y a/\sqrt{3}} + e^{-ik_y a/2\sqrt{3}}(\frac{t_3}{t_1}e^{ik_x a/2} + \frac{t_2}{t_1}e^{-ik_x a/2})]$, where $t_1 = 2.7$ eV and $t_2 = t_3 = 1.35$ eV are the anisotropic hopping energies with $a = 2.46$ Å as the lattice constant. The above Hamiltonian results in an energy landscape characteristic of a semi-Dirac semimetal, exhibiting linear dispersion along k_x and quadratic dispersion along k_y, as evident in Figs. 1(a) and 1(b), respectively. The interaction of an intense laser pulse with the semi-Dirac system is modeled within the density-matrix formalism by solving the semiconductor Bloch equations in the Houston basis as [66,69]

$$i\partial_t \rho^{\mathbf{k}}_{mn}(t) = \left(\mathcal{E}^{\mathbf{k}+\mathbf{A}(t)}_{mn} + \frac{(1-\delta_{mn})}{T_2}\right)\rho^{\mathbf{k}}_{mn}(t) + \mathbf{F}(t)\cdot\sum_{n'}\left[\rho^{\mathbf{k}}_{mn'}(t)\mathbf{d}^{\mathbf{k}+\mathbf{A}(t)}_{n'n} - \mathbf{d}^{\mathbf{k}+\mathbf{A}(t)}_{mn'}\rho^{\mathbf{k}}_{n'n}(t)\right]. \tag{2}$$

This time-dependent equation is solved numerically using a fourth-order Runge-Kutta method with a time step of 0.02 fs. The Brillouin zone is discretized on a 200×200 $\mathbf{k}$-point grid to ensure convergence of the calculated observables. The energy difference between bands m and n is denoted by $\mathcal{E}_{mn}$, whereas $\mathbf{d}^{\mathbf{k}+\mathbf{A}(t)}_{mn}$ represents the matrix element evaluated at the crystal momentum shifted by the laser vector potential $\mathbf{A}(t)$. $\mathbf{F}(t)$ is the driving electric field and ρ_{mn} denotes the density matrix component between m and n energy bands. Dissipative effects are incorporated via a phenomenological dephasing time $T_2 = 10$ fs. The main conclusions remain robust for dephasing times between 3 and 20 fs (see Supplemental Material [70]). The high-harmonic spectra are computed from the total time-dependent current $\mathbf{J}(t)$ as $\mathcal{I}(\omega) = |\mathcal{FT}(\partial\mathbf{J}(t)/\partial t)|^2$, where $\mathcal{FT}$ denotes the Fourier transform.

We express the vector potential of the elliptically polarized laser pulse with ellipticity ϵ as

$$\mathbf{A}(t) = \frac{g(t)A_0}{\sqrt{1+\epsilon^2}}[\cos(\omega t)\hat{\mathbf{e}}_x + \epsilon\sin(\omega t)\hat{\mathbf{e}}_y]. \tag{3}$$

Here, $g(t)$ is the envelope of the laser pulse, A_0 is the amplitude of the vector potential, and ω is the frequency of the driving laser pulse. $\epsilon = 1$ and -1 correspond to right-handed and left-handed circularly polarized light, respectively, while $\epsilon = 0$ is a linearly polarized pulse polarized along the k_x direction. In this work, the driving laser pulse is centered at 3200 nm, a pulse duration of approximately 100 fs with a sin-squared temporal envelope, and a peak intensity of 1×10^{11} W/cm^2. The polarization state of the laser is systematically varied from linear to circular, and its orientation is rotated with respect to the crystalline axes—from alignment along high-symmetry directions to arbitrary in-plane angles—allowing for a comprehensive mapping of anisotropic nonlinear responses.

III. RESULTS AND DISCUSSION

Figures 1(c) and 1(d) present the high-harmonic spectra of the semi-Dirac system for linearly and circularly polarized laser pulses, respectively. Owing to the inversion symmetry, a semi-Dirac semimetal exclusively emits odd-order harmonics as evident from Fig. 1(c). These harmonics are generated along the polarization direction of the incident laser. Additionally, a semi-Dirac semimetal exhibits a complex interplay between intraband and interband contributions, a signature of the semimetal systems. A pronounced enhancement in the efficiency of the emitted harmonics is observed as the polarization direction of the driving pulse is varied from k_x to k_y. To elucidate the pronounced enhancement of the harmonic yield for laser polarization along the k_y direction, we analyze the dipole coupling, which determines the strength of interband transitions and, consequently, the efficiency of harmonic emission. The dipole coupling exhibits strong anisotropy across the first Brillouin zone, as shown in Fig. 2. In particular, the interband dipole matrix elements are significantly enhanced in the vicinity of the high-symmetry point M and along the K-M-K' path. This behavior originates from the vanishing band gap along the k_y direction, which facilitates a strong interband excitation and enhances the interband contribution to the harmonic signal. In contrast, for laser polarization along the k_x direction, the larger band gap suppresses interband transitions, leading to a comparatively weaker harmonic response. The anisotropic band dispersion of the semi-Dirac system therefore results in direction-dependent coupling between valence and conduction bands, giving rise to strongly enhanced harmonic emission for driving the laser along the k_y direction.

The emission characteristics change significantly when the laser polarization is varied from linear to circular, as shown in Fig. 1(d). As discussed above, the anisotropic band dispersion of the semi-Dirac semimetal is closely connected to the underlying lattice symmetry. The intrinsic twofold rotational symmetry gives rise to well-defined selection rules, resulting in the generation of circular harmonics that follow the characteristic $(2n \pm 1)$-order sequence, with contributions from both left- and right-handed helicities. Remarkably, the semi-Dirac semimetal exhibits a clean spectrum consisting exclusively of odd-order harmonics, extending well beyond the ninth order under circularly polarized excitation. Even more strikingly, the harmonic yield is enhanced by several orders of magnitude compared to the response obtained for linearly polarized light along the k_x direction. This pronounced enhancement stands in sharp contrast to previous studies on two-dimensional

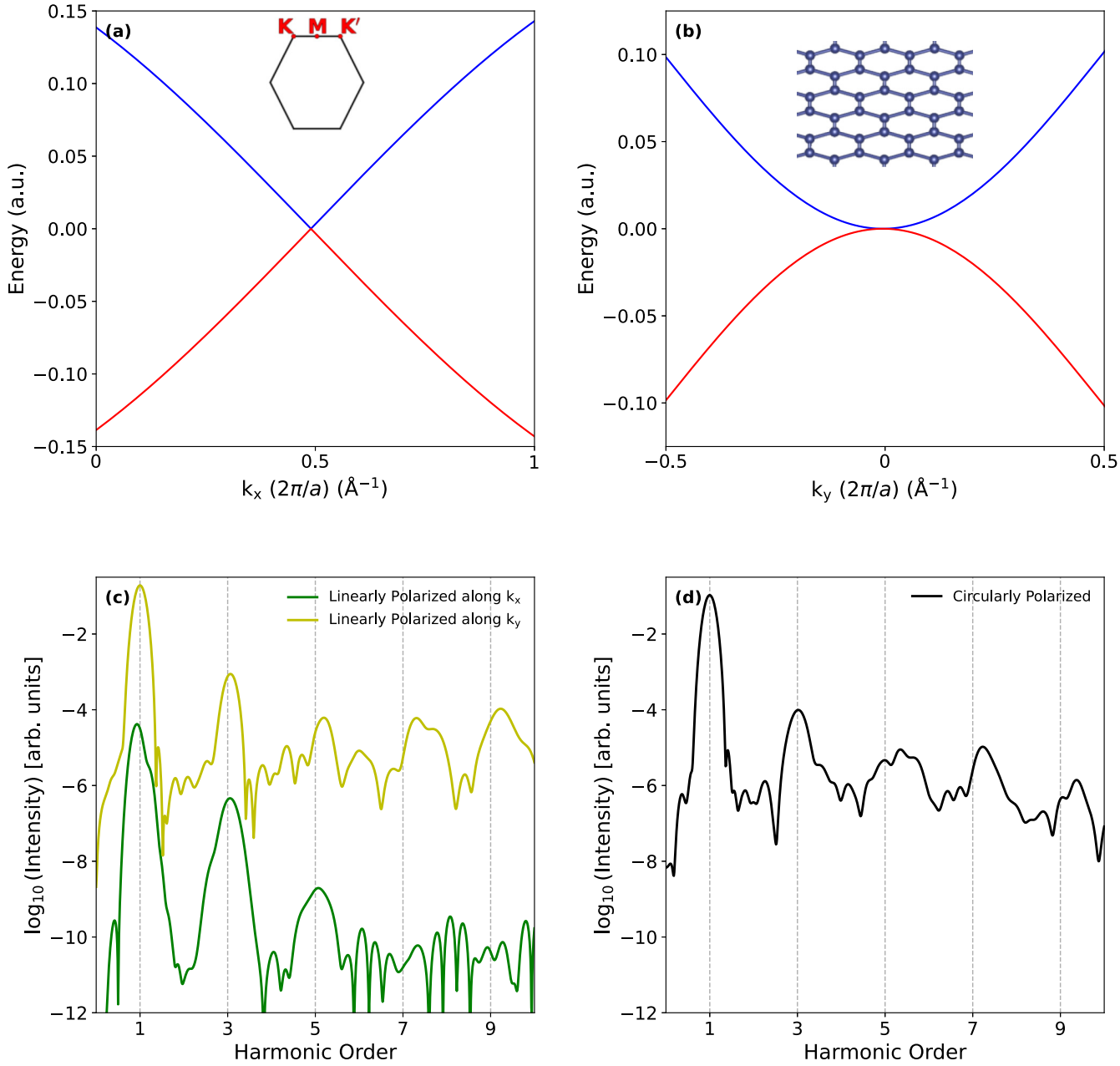


FIG. 1. Energy dispersion of a two-dimensional semi-Dirac system along the (a) k_x and (b) k_y directions in the vicinity of the high-symmetry point M. High-harmonic spectra for (c) linearly polarized pulses along the k_x and k_y directions, and (d) a circularly polarized pulse in the k_x-k_y plane. The real-space lattice structure of the semi-Dirac system, exhibiting twofold rotational symmetry, is visible in the inset of (b). High-symmetry points within the first Brillouin zone of the semi-Dirac system is shown in the inset of (a).

semimetals, which reported suppressed harmonic yields under circular polarization.

To gain deeper insight into the microscopic origin of the enhanced harmonic yield under circularly polarized excitation, we analyze the momentum-resolved harmonic intensity, $\mathcal{I}(\mathbf{k}, \omega)$, as shown in Fig. 3. The total time-dependent electronic current $\mathbf{J}(t)$ arises from the cumulative contribution of microscopic currents distributed over reciprocal-space points within the first Brillouin zone, and can be expressed as $\mathbf{J}(t) = \int_{\mathrm{BZ}} \mathbf{J}(\mathbf{k}, t) d\mathbf{k}$. Accordingly, the harmonic response can be analyzed in a momentum-resolved manner by examining the local current at each $\mathbf{k}$ point. In particular, the momentum-resolved harmonic intensity, $\mathcal{I}(\mathbf{k}, \omega)$, is obtained from the squared modulus of the Fourier transform of the time derivative of the microscopic current, $|\mathcal{FT}[\partial \mathbf{J}(\mathbf{k}, t)/\partial t]|^2$. This formulation provides a direct mapping of how microscopic current dynamics across the Brillouin zone contribute to the overall harmonic emission.

The dominant contributions to the harmonic emission arise from regions in the vicinity of the high-symmetry points M, K, and K' within the first Brillouin zone. In particular, the strong dipole coupling near the M point leads to a substantial contribution to the harmonic signal, reflecting the enhanced interband transition probability in this region. As the harmonic order increases, the corresponding distribution in momentum space expands progressively, covering a larger

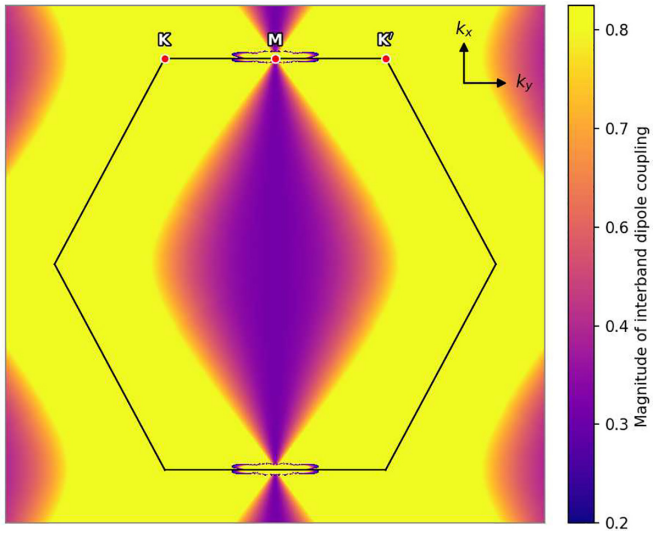


FIG. 2. The dipole coupling for a semi-Dirac system in the first Brillouin zone. The dipole coupling is more significant in the vicinity of M and along K-M-K'. The interband dipole couple strength is estimated as $\mathbf{d}^{\mathbf{k}}_{mn} = i\mathbf{p}^{\mathbf{k}}_{mn}/\mathcal{E}^{\mathbf{k}}_{mn}$ with $\mathbf{p}^{\mathbf{k}}$ as the momentum matrix element.

region of the Brillouin zone. This behavior indicates that higher-order harmonics originates farther away from the band extrema, where carriers experience larger excursions in momentum space under the influence of the circularly polarized field. The optical excitations happen at the $\mathbf{k}$ points where the energy gap is equal to the photon energy. The interband contribution of the nth harmonic will be dominantly from $\mathbf{k}$ points satisfying $\mathcal{E}_{cv} = E_c(\mathbf{k}) - E_v(\mathbf{k}) = n\hbar\omega$. The stronger color intensity away from the energy contour of $n\hbar\omega$ in Fig. 3 signifies the contribution from intraband dynamics. Moreover, the extended momentum-space distribution for higher harmonics reflects the increasing role of nonlinear intraband motion, which drives carriers across broader regions of the band structure before recombination. The combined effect of strong interband dipole coupling near the high-symmetry points and anisotropic intraband acceleration leads to efficient harmonic emission.

We also investigate the time-frequency maps of the emitted harmonics at individual high-symmetry points (K, M, and K') and compare the results with those of the well-known two-dimensional Dirac semimetal, graphene. Pronounced higher-order harmonic emission is observed at the K, M, and K' points in the semi-Dirac system, as shown in Figs. 4(a)–4(c). Notably, the high-harmonic bursts originating from the K and K' points exhibit a phase difference of π, as evident from Figs. 4(b) and 4(c). Specifically, when the y component of the circularly polarized driving field reaches its maximum value, the dominant contribution to the harmonic emission arises from the K' point. In contrast, when the y component of the field attains its minimum value, the K point predominantly contributes to the emission.

In contrast to the semi-Dirac system, the dominant harmonic contributions in graphene primarily originate from the vicinity of the K and K' points. Moreover, the emissions from these two points are out of phase, leading to partial cancellation and consequently a reduced overall harmonic intensity for circularly polarized driver. These emissions occur as the y component of the electric field evolves between its minimum and maximum values. At the M point, the semi-Dirac system exhibits the strongest harmonic emission, as shown in Fig. 4(a), consistent with the enhanced dipole coupling at this high-symmetry location. However, graphene shows no significant harmonic emission beyond the third order at the M point due to the comparatively weaker dipole coupling, as illustrated in Fig. 4(d). The overall features closely resemble those observed in the momentum-resolved harmonic spectra. Furthermore, the higher-order harmonic bursts in the semi-Dirac semimetal appear at later times relative to the lower-order harmonics, indicating the presence of a positive chirp in the harmonic generation process.

The generation of high-order harmonics driven by a circularly polarized laser field does not necessarily imply that the emitted harmonics are purely circularly polarized. The presence of both left- and right-handed helicity components contributing to each harmonic order can modify the ellipticity of the emitted harmonics. To characterize the polarization properties of the emitted radiation, we extract the time-domain signals corresponding to the third (H3), fifth (H5), seventh (H7), and ninth (H9) harmonics from the time-dependent current, as shown in Fig. 5. The polarization state of each harmonic is then quantified by computing the ellipticity from the orthogonal components of the emitted field. The calculated ellipticities for H3, H5, H7, and H9 are 0.48, 0.34, 0.88, and 0.85, respectively, indicating that the emitted harmonics are predominantly elliptically polarized even when driven by a circularly polarized laser field. The deviation from perfect circular polarization originates from the anisotropic band structure of the semi-Dirac system, which leads to unequal contributions from the two helicity channels and induces mixing between orthogonal current components. In particular, the interplay between interband coherence and intraband motion modifies the relative phase and amplitude of the orthogonal field components, resulting in elliptically polarized harmonic emission. Importantly, we verify that the qualitative behavior of the harmonic ellipticity remains robust with respect to the choice of the dephasing time as presented in the Supplemental Material [70]. These findings demonstrate that the polarization properties of the emitted harmonics are governed primarily by the intrinsic symmetry and anisotropic dispersion of the semi-Dirac system rather than by relaxation effects.

Having established the semi-Dirac system as an efficient source of high-order harmonics with tunable ellipticity, and following a comparison of its dynamical response with that of monolayer graphene, we now investigate the dependence of the HHG response on the ellipticity of the driving field. Figure 6 illustrates the pronounced sensitivity of the harmonic yield to the ellipticity. Both left-handed ($\epsilon < 0$) and right-handed ($\epsilon > 0$) helicities exhibit identical behavior. The overall harmonic yield remains minimal under linear polarization but increases significantly as the ellipticity approaches circular polarization in the semi-Dirac system, as shown in Fig. 6. For H3, the total yield exhibits a local minimum around $\epsilon \approx 0.45$, followed by a sharp increase that reaches its maximum at circular polarization, $\epsilon = \pm 1$. In contrast, for graphene the harmonic yield attains its maximum near $\epsilon \approx 0.2$, after which it decreases substantially and becomes nearly negligible as ϵ approaches ± 1. Similar behavior is observed

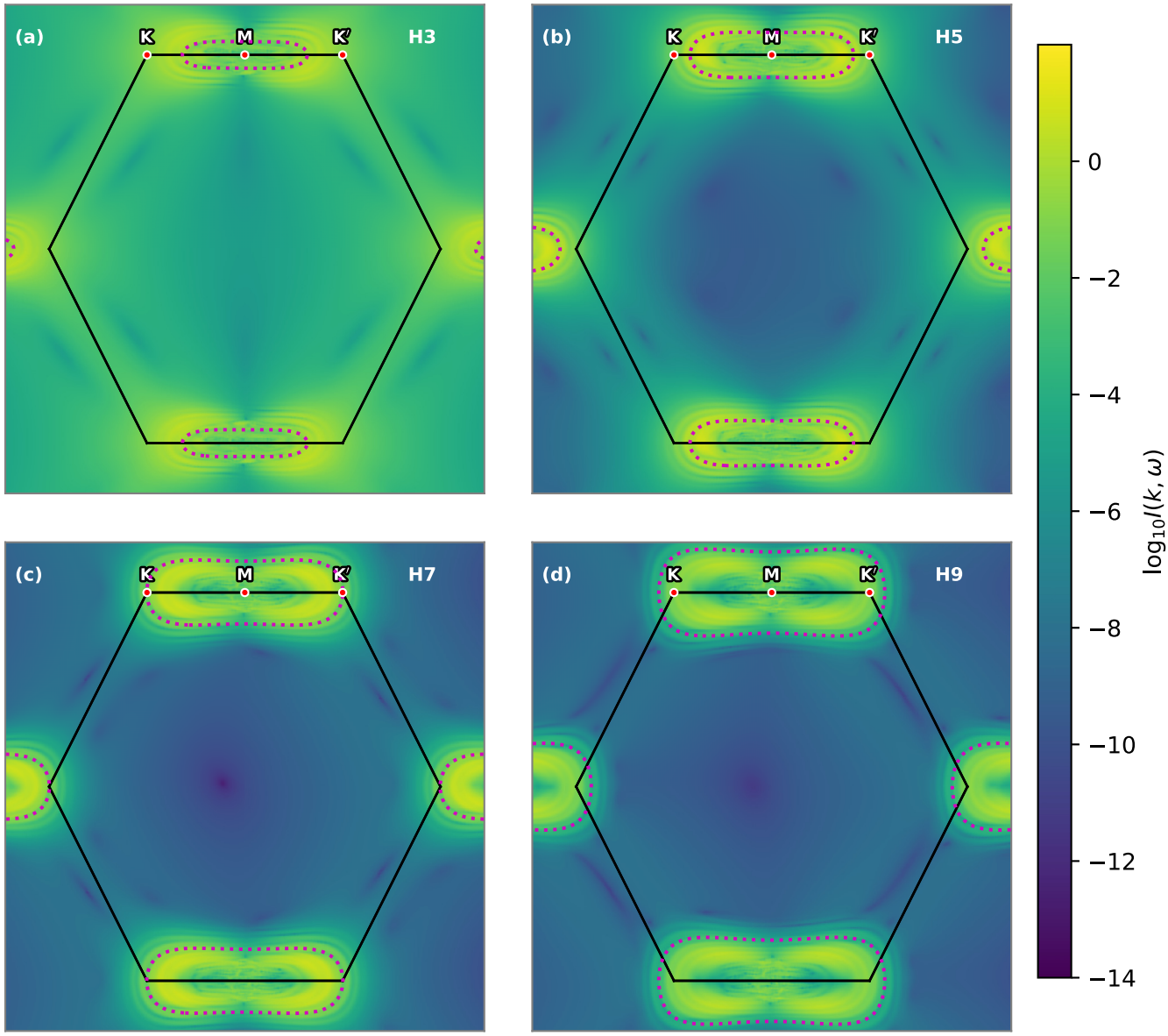


FIG. 3. Momentum-resolved (a) third (H3), (b) fifth (H5), (c) seventh (H7), and (d) ninth (H9) harmonics for the circularly polarized driving laser in the first Brillouin zone. The purple dashed lines reveal the contours defined by $E_c(\mathbf{k}) - E_v(\mathbf{k}) = n\hbar\omega$, where n is the harmonic order.

for H5 and H7 in graphene, where the harmonic yield peaks near $\epsilon \approx 0.25$ and subsequently decreases with increasing ellipticity. This anomalous ellipticity dependence in graphene is consistent with previous experimental observations [29].

For the semi-Dirac system, H5 exhibits a suppression of the total yield around $\epsilon \approx 0.35$, followed by a pronounced maximum near $\epsilon \approx 0.7$, before decreasing at higher ellipticities, as shown in Fig. 6(b). In contrast, H7 displays an almost monotonic increase in the total yield with increasing ellipticity, apart from a minor deviation around $\epsilon \approx 0.5$, reaching its maximum at circular polarization [Fig. 6(c)]. These results demonstrate that efficient harmonic generation in the semi-Dirac system can be achieved by tuning the ellipticity of the driving field, with near-circular polarization yielding significantly enhanced harmonic intensities, particularly for H3 and H7. These distinct ellipticity dependencies arise from the anisotropic energy dispersion and the enhanced dipole coupling along the k_y direction. Present ellipticity sensitivities stand in stark contrast to those reported for pristine graphene and nodal-line semimetals, where the harmonic yield exhibits anomalous ellipticity dependence and is strongly suppressed under circularly polarized excitation [65,66]. We note that similar trends are observed even when different values of the dephasing time are considered, as demonstrated in the Supplemental Material [70].

It is important to emphasize that the integrated harmonic yield exhibits a monotonic dependence on the laser ellipticity in gapped semi-Dirac systems. The anomalous enhancement of the harmonic yield emerges only in the gapless semi-Dirac system. Furthermore, the dipole coupling is no longer strongly localized around the M point—the band-touching point of the gapless system—but becomes more

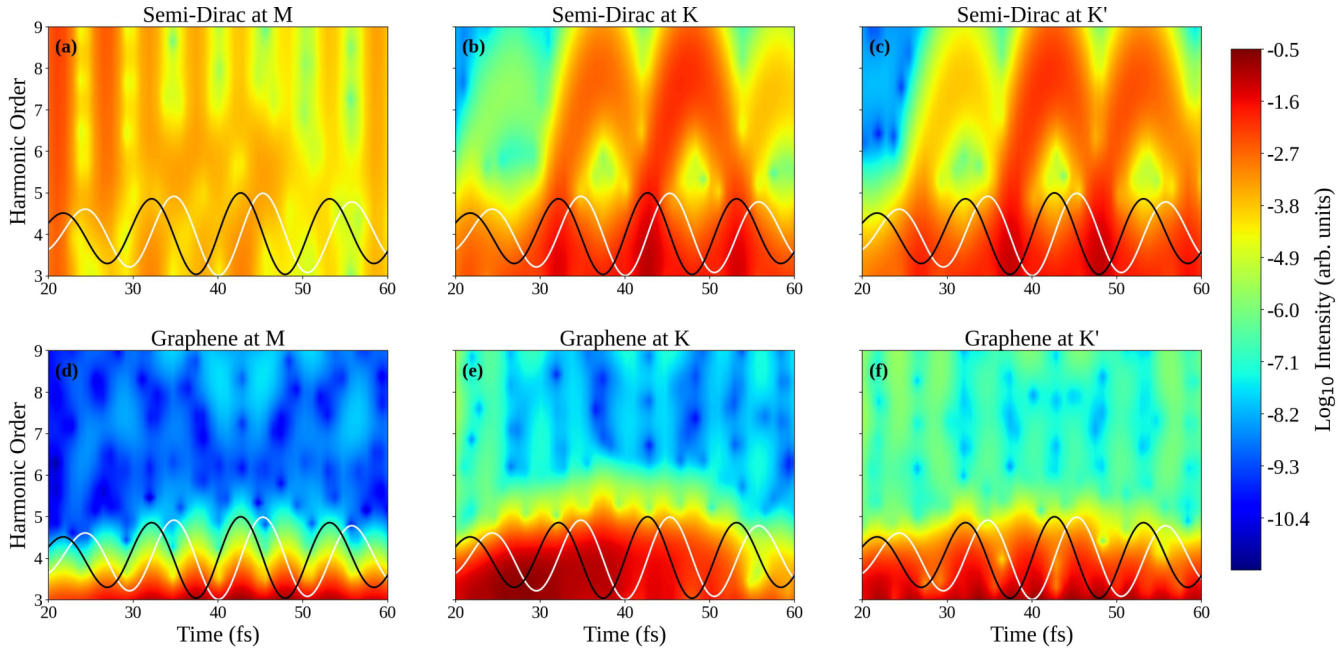


FIG. 4. Time-frequency maps at the (a) M, (b) K, and (c) K' points of the semi-Dirac semimetal. (d)–(f) show the corresponding results for monolayer graphene. The white and black lines denote the x and y components of the circularly polarized driving field, respectively.

broadly distributed throughout the Brillouin zone. As a result, the unique enhancement arising from the highly anisotropic electronic structure is significantly suppressed. These observations provide compelling evidence that the anomalous harmonic enhancement is an intrinsic consequence of the gapless semi-Dirac band topology and the associated anisotropic dipole coupling.

To gain deeper insight into the role of the underlying symmetry of the system to the nonperturbative nonlinear response, let us analyze how HHG is sensitive to the polarization direction of the incident laser. The sensitivity of the laser's polarization to the H3, H5, H7, and H9 harmonics is presented in Fig. 7. All harmonics exhibit anisotropic responses, with H3, H5, and H9 displaying twofold maxima at $\theta = 90^\circ$ and 270°, while H7 exhibits suppression at $\theta = 90^\circ$ and 270° and maxima at $\theta \approx 60^\circ$, 120°, 240° and 300°. Notably, harmonic yields are strongly suppressed along the k_x direction, and H5 and H7 exhibit distinct polarization angles corresponding to their respective maxima and minima. The maxima in the polarization harmonic yields can also be attributed to the electron hopping between neighboring atoms when the laser is polarized along the direction connecting them. In particular, H3 and H5 primarily emerge from nearest-neighbor contributions, whereas H7 arises from next-nearest-neighbor interactions, as illustrated in Figs. 7(a)–7(c). From the lattice structure shown in the inset of Fig. 1(b), the maximum harmonic yield is expected to occur along 30° and 90° when only nearest-neighbor interactions are considered. This behavior is consistent with the polarization-resolved profiles of H3 and H5 presented in Figs. 7(a) and 7(b). However, the maximum yield is observed to shift toward 60° for H7 as illustrated in Fig. 7(c). This deviation indicates the significant contribution of second-nearest-neighbor interactions, which must be included to accurately capture the polarization dependence. These anisotropic features can thus be understood as a consequence of the twofold symmetry of the lattice and the contrasting linear and quadratic band dispersions along the k_x and k_y directions, respectively. Such dispersion asymmetry leads to directionally dependent interband transitions, manifesting as polarization-sensitive harmonic yields. The Present findings highlight the crucial role of lattice symmetry and energy dispersion in governing HHG characteristics, with the semi-Dirac system providing a compelling platform for exploring anisotropic light-matter interactions [71].

In summary, we have explored how semi-Dirac fermions imprint their distinctive signatures in the high-harmonic spectra. Our results reveal a rich interplay between lattice symmetry, anisotropic band dispersion, and the polarization of the driving laser pulse, collectively shaping the nonlinear nonperturbative optical response of these systems. Owing to inversion symmetry, the system supports only odd-order harmonic emission, while the twofold rotational symmetry induced by anisotropy enables all odd-order circular harmonics. Remarkably, circularly polarized excitation—typically known to suppress HHG in two-dimensional semimetals—enhances the harmonic yield in semi-Dirac semimetals by several orders of magnitude. The enhanced efficiency of circular harmonics can be attributed to the stronger dipole coupling along the k_y direction compared to k_x, with dominant contributions emerging from high-symmetry points, particularly the M point. Furthermore, time-domain analysis of the emitted harmonics reveals that the third, fifth, seventh, and ninth harmonics possess ellipticities of 0.48, 0.34, 0.88, and 0.85, respectively, indicating that higher-order harmonics approach near-circular polarization under circularly polarized driving fields. Momentum-resolved and time-frequency analyses further show that higher-order harmonics originate from extended regions of the Brillouin zone and exhibit delayed emission with positive chirp, reflecting underlying electron wave-packet dynamics.

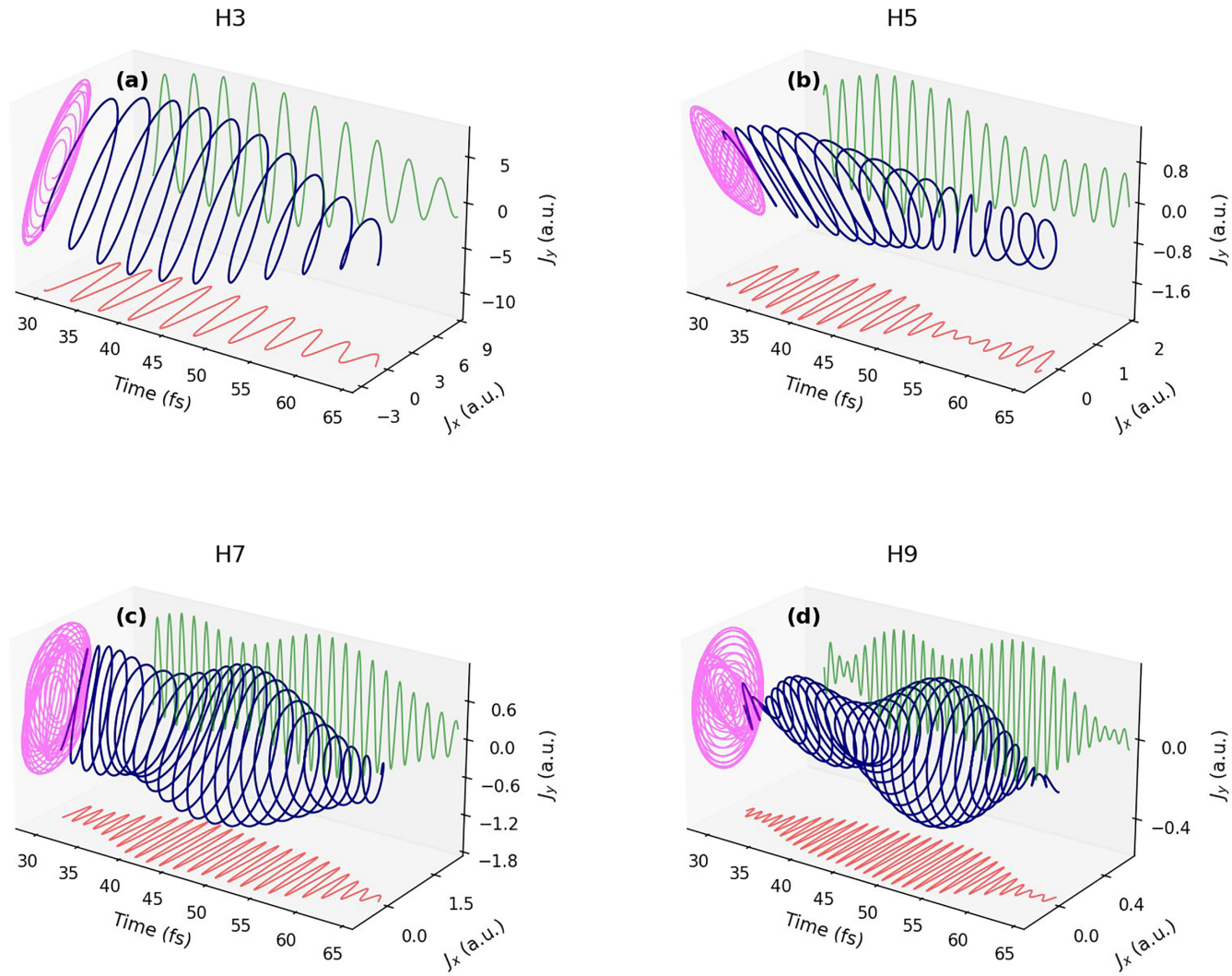


FIG. 5. Time-domain signals of the (a) H3, (b) H5, (c) H7, and (d) H9 harmonics driven by a circularly polarized laser field. The blue curve shows the total harmonic signal, while the red and orange curves represent its x and y components, respectively. The magenta curves display the corresponding Lissajous figures used to characterize the polarization state of each harmonic.

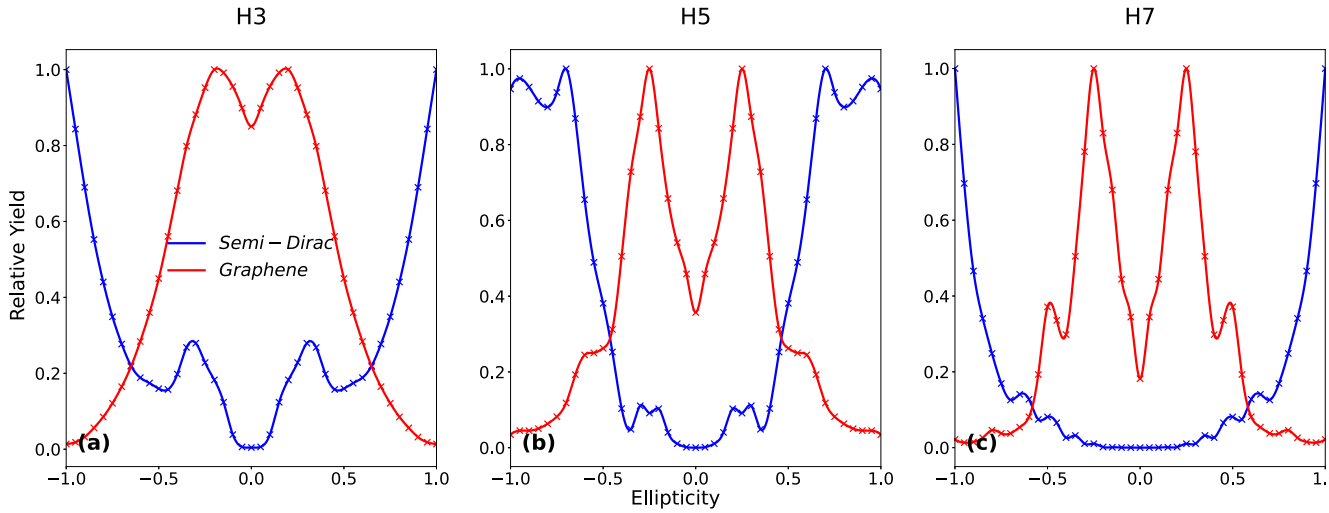


FIG. 6. Integrated harmonic yield as a function of the driving laser ellipticity for (a) H3, (b) H5, and (c) H7 harmonics, with the major axis of the driving pulse aligned along the k_x direction. For each ellipticity, the yield is normalized with respect to the maximum value of the yield. Red and blue curves denote the normalized total harmonic yields for graphene and the Semi-Dirac system, respectively.

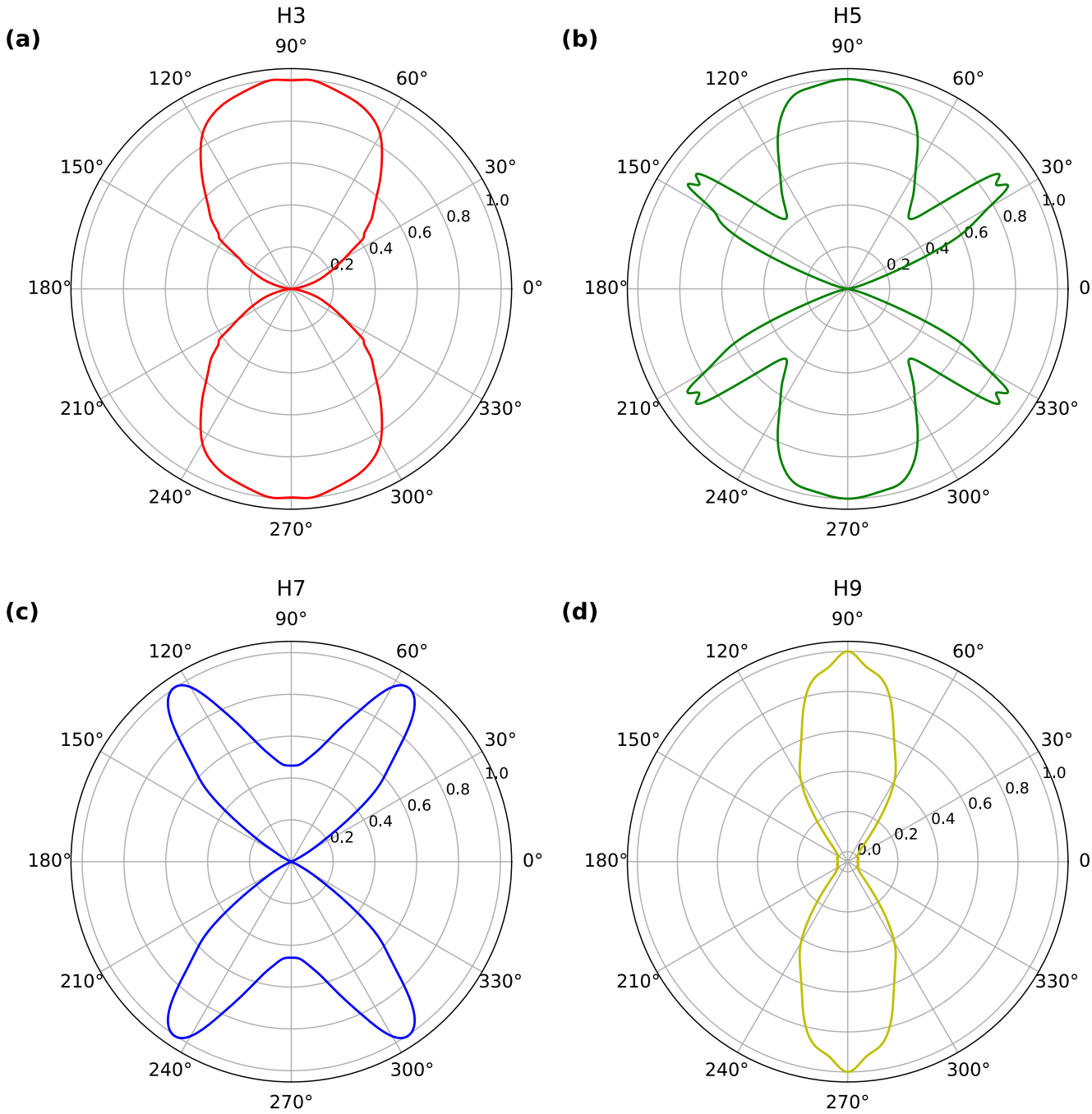


FIG. 7. Polarization-direction sensitivity of the normalized harmonic yield for (a) H3, (b) H5, (c) H7, and (d) H9 harmonics generated from a semi-Dirac system. All yields are normalized to their respective maxima to enable direct comparison.

Ellipticity dependence reveals a pronounced sensitivity of the harmonic yield to the driving field's polarization: the total yield is minimal for linear polarization along the k_x direction and increases sharply toward circular polarization, with harmonic-specific nonmonotonic trends. A comparative analysis with graphene highlights a striking contrast, where harmonic emission is strongly suppressed under circular polarization due to destructive interference between contributions from K and K' points, whereas in the semi-Dirac system, constructive contributions—particularly near the M point—lead to substantial enhancement. Polarization-resolved measurements further unveil distinct anisotropies, including twofold and fourfold angular patterns, arising from the coexistence of linear and quadratic dispersions along orthogonal momentum directions. These distinctive trends persist across a broad range of driving conditions, underscoring both the robustness and the potential universality of our findings as illustrated in the Supplemental Material [70]. Present findings establish the semi-Dirac semimetal as a promising platform for symmetry-engineered and anisotropy-enhanced HHG, offering potential avenues for controlling strong-field processes in solids through tailored band structures, momentum-space engineering, and light polarization.

ACKNOWLEDGMENT

We are thankful for useful discussion with Dr. Navdeep Rana.

DATA AVAILABILITY

The data that support the findings of this article are openly available [72], embargo periods may apply.

[1] D. N. Basov, R. D. Averitt, and D. Hsieh, Towards properties on demand in quantum materials, Nat. Mater. **16**, 1077 (2017).

[2] N. P. Armitage, E. J. Mele, and A. Vishwanath, Weyl and Dirac semimetals in three-dimensional solids, Rev. Mod. Phys. **90**, 015001 (2018).

[3] C. Bao, P. Tang, D. Sun, and S. Zhou, Light-induced emergent phenomena in 2D materials and topological materials, Nat. Rev. Phys. **4**, 33 (2022).

[4] A. Bharti, M. Ivanov, and G. Dixit, How massless are Weyl fermions in Weyl semimetals, Phys. Rev. B **108**, L020305 (2023).

[5] J. W. McIver, D. Hsieh, H. Steinberg, P. Jarillo-Herrero, and N. Gedik, Control over topological insulator photocurrents with light polarization, Nat. Nanotechnol. **7**, 96 (2012).

[6] B. Yan and C. Felser, Topological materials: Weyl semimetals, Annu. Rev. Condens. Matter Phys. **8**, 337 (2017).

[7] A. Bharti and G. Dixit, Photocurrent generation in solids via linearly polarized laser, Phys. Rev. B **109**, 104309 (2024).

[8] M. U. Farooq, A. Hashmi, M. Tani, K. Yabana, K. L. Ishikawa, L. Huang, and T. Otobe, Nonlinear Hall effect in bilayer WTe_2 induced by strong laser fields, Phys. Rev. B **112**, 035143 (2025).

[9] N. S. Sirica and R. P. Prasankumar, Shaking up topology with light, Nat. Mater. **20**, 283 (2021).

[10] F. Qin, R. Chen, and C. H. Lee, Light-enhanced nonlinear Hall effect, Commun. Phys. **7**, 368 (2024).

[11] F. Krausz and M. Ivanov, Attosecond physics, Rev. Mod. Phys. **81**, 163 (2009).

[12] S. Ghimire, A. D. DiChiara, E. Sistrunk, P. Agostini, L. F. DiMauro, and D. A. Reis, Observation of high-order harmonic generation in a bulk crystal, Nat. Phys. **7**, 138 (2011).

[13] C. Heide, Y. Kobayashi, D. R. Baykusheva, D. Jain, J. A. Sobota, M. Hashimoto, P. S. Kirchmann, S. Oh, T. F. Heinz, D. A. Reis, *et al.*, Probing topological phase transitions using high-harmonic generation, Nat. Photon. **16**, 620 (2022).

[14] M. S. Mrudul, A. Pattanayak, M. Ivanov, and G. Dixit, Direct numerical observation of real-space recollision in high-order harmonic generation from solids, Phys. Rev. A **100**, 043420 (2019).

[15] N. Saito, P. Xia, F. Lu, T. Kanai, J. Itatani, and N. Ishii, Observation of selection rules for circularly polarized fields in high-harmonic generation from a crystalline solid, Optica **4**, 1333 (2017).

[16] K. Kaneshima, Y. Shinohara, K. Takeuchi, N. Ishii, K. Imasaka, T. Kaji, S. Ashihara, K. L. Ishikawa, and J. Itatani, Polarization-resolved study of high harmonics from bulk semiconductors, Phys. Rev. Lett. **120**, 243903 (2018).

[17] M. Borsch, C. P. Schmid, L. Weigl, S. Schlauderer, N. Hofmann, C. Lange, J. T. Steiner, S. W. Koch, R. Huber, and M. Kira, Super-resolution lightwave tomography of electronic bands in quantum materials, Science **370**, 1204 (2020).

[18] G. Vampa, T. J. Hammond, N. Thiré, B. E. Schmidt, F. Légaré, C. R. McDonald, T. Brabec, D. D. Klug, and P. B. Corkum, All-optical reconstruction of crystal band structure, Phys. Rev. Lett. **115**, 193603 (2015).

[19] C. P. Schmid, L. Weigl, P Grössing, V. Junk, C. Gorini, S. Schlauderer, S. Ito, M. Meierhofer, N. Hofmann, D. Afanasiev, *et al.*, Tunable non-integer high-harmonic generation in a topological insulator, Nature (London) **593**, 385 (2021).

[20] C. Qian, C. Yu, S. Jiang, T. Zhang, J. Gao, S. Shi, H. Pi, H. Weng, and R. Lu, Role of shift vector in high-harmonic generation from noncentrosymmetric topological insulators under strong laser fields, Phys. Rev. X **12**, 021030 (2022).

[21] L. Yue and M. B. Gaarde, Imperfect recollisions in high-harmonic generation in solids, Phys. Rev. Lett. **124**, 153204 (2020).

[22] M. S. Mrudul, N. Tancogne-Dejean, A. Rubio, and G. Dixit, High-harmonic generation from spin-polarised defects in solids, npj Comput. Mater. **6**, 10 (2020).

[23] H. Lakhotia, H. Y. Kim, M. Zhan, S. Hu, S. Meng, and E. Goulielmakis, Laser picoscopy of valence electrons in solids, Nature (London) **583**, 55 (2020).

[24] A. Pattanayak, M. S. Mrudul, and G. Dixit, Influence of vacancy defects in solid high-order harmonic generation, Phys. Rev. A **101**, 013404 (2020).

[25] S. Ghimire and D. A. Reis, High-harmonic generation from solids, Nat. Phys. **15**, 10 (2019).

[26] J. Alcalà, U. Bhattacharya, J. Biegert, M. Ciappina, U. Elu, T. Graß, P. T. Grochowski, M. Lewenstein, A. Palau, T. P. H. Sidiropoulos, *et al.*, High-harmonic spectroscopy of quantum phase transitions in a high-Tc superconductor, Proc. Natl. Acad. Sci. USA **119**, e2207766119 (2022).

[27] L. Li, P. Lan, X. Zhu, and P. Lu, High harmonic generation in solids: Particle and wave perspectives, Rep. Prog. Phys. **86**, 116401 (2023).

[28] C. Heide, Y. Kobayashi, S. R. Ul Haque, and S. Ghimire, Ultrafast high-harmonic spectroscopy of solids, Nat. Phys. **20**, 1546 (2024).

[29] N. Yoshikawa, T. Tamaya, and K. Tanaka, High-harmonic generation in graphene enhanced by elliptically polarized light excitation, Science **356**, 736 (2017).

[30] S. Cha, M. Kim, Y. Kim, S. Choi, S. Kang, H. Kim, S. Yoon, G. Moon, T. Kim, Y. W. Lee, *et al.*, Gate-tunable quantum pathways of high harmonic generation in graphene, Nat. Commun. **13**, 6630 (2022).

[31] H. K. Avetissian, G. F. Mkrtchian, and A. Knorr, Efficient high-harmonic generation in graphene with two-color laser field at orthogonal polarization, Phys. Rev. B **105**, 195405 (2022).

[32] Y. Murakami and M. Schüler, Doping and gap size dependence of high-harmonic generation in graphene: Importance of consistent formulation of light-matter coupling, Phys. Rev. B **106**, 035204 (2022).

[33] F. Dong, Q. Xia, and J. Liu, Ellipticity of the harmonic emission from graphene irradiated by a linearly polarized laser, Phys. Rev. A **104**, 033119 (2021).

[34] Y. Zhang, L. Li, J. Li, T. Huang, P. Lan, and P. Lu, Orientation dependence of high-order harmonic generation in graphene, Phys. Rev. A **104**, 033110 (2021).

[35] R. Boyero-García, A. García-Cabrera, O. Zurrón-Cifuentes, C. Hernández-García, and L. Plaja, Non-classical high harmonic generation in graphene driven by linearly-polarized laser pulses, Opt. Express **30**, 15546 (2022).

[36] Z. Guan, Z. Yin, J. You, B. Wang, X. Li, G.-L. Wang, X.-X. Zhou, and C. Jin, Optimal generation and systematic analysis of tunable terahertz emissions from single-layer graphene using two-color laser pulses with different durations, Phys. Rev. A **108**, 023515 (2023).

[37] N. Rana, M. S. Mrudul, D. Kartashov, M. Ivanov, and G. Dixit, High-harmonic spectroscopy of coherent lattice dynamics in graphene, Phys. Rev. B **106**, 064303 (2022).

[38] F. Dong and J. Liu, Knee structure in the laser-intensity dependence of harmonic generation for graphene, Phys. Rev. A **106**, 043103 (2022).

[39] Ó. Zurrón-Cifuentes, R. Boyero-García, C. Hernández-García, A. Picón, and L. Plaja, Optical anisotropy of non-perturbative high-order harmonic generation in gapless graphene, Opt. Express **27**, 7776 (2019).

[40] M. S. Mrudul, Dependence of high-harmonic generation in twisted bilayer graphene on laser pulse ellipticity, Phys. Rev. B **110**, 115415 (2024).

[41] Ó. Zurrón, A. Picón, and L. Plaja, Theory of high-order harmonic generation for gapless graphene, New J. Phys. **20**, 053033 (2018).

[42] C. Liu, Y. Zheng, Z. Zeng, and R. Li, Driving-laser ellipticity dependence of high-order harmonic generation in graphene, Phys. Rev. A **97**, 063412 (2018).

[43] S. A. Sørngård, S. I. Simonsen, and J. P. Hansen, High-order harmonic generation from graphene: Strong attosecond pulses with arbitrary polarization, Phys. Rev. A **87**, 053803 (2013).

[44] L. A. Chizhova, F. Libisch, and J. Burgdörfer, Nonlinear response of graphene to a few-cycle terahertz laser pulse: Role of doping and disorder, Phys. Rev. B **94**, 075412 (2016).

[45] H. K. Avetissian, A. K. Avetissian, G. F. Mkrtchian, and K. V. Sedrakian, Creation of particle-hole superposition states in graphene at multiphoton resonant excitation by laser radiation, Phys. Rev. B **85**, 115443 (2012).

[46] H. K. Avetissian and G. F. Mkrtchian, Impact of electron-electron Coulomb interaction on the high harmonic generation process in graphene, Phys. Rev. B **97**, 115454 (2018).

[47] Z.-Y. Li, Q. Li, and Z. Li, High-order harmonic generations in tilted Weyl semimetals, Chin. Phys. B **31**, 124204 (2022).

[48] A. Bharti and G. Dixit, Non-perturbative nonlinear optical responses in Weyl semimetals, Appl. Phys. Lett. **125**, 051104 (2024).

[49] H. K. Avetissian, V. N. Avetisyan, B. R. Avchyan, and G. F. Mkrtchian, High-order harmonic generation in three-dimensional Weyl semimetals with broken time-reversal symmetry, Phys. Rev. A **106**, 033107 (2022).

[50] Y.-Y. Lv, J. Xu, S. Han, C. Zhang, Y. Han, J. Zhou, S.-H. Yao, X.-P. Liu, M.-H. Lu, H. Weng, *et al.*, High-harmonic generation in Weyl semimetal β-WP_2 crystals, Nat. Commun. **12**, 6437 (2021).

[51] L. Wang, M. F. Ciappina, T. Brabec, and X. J. Liu, Tabletop tunable chiral photonic emitter, Phys. Rev. Lett. **133**, 113804 (2024).

[52] S. Kovalev, R. M. A. Dantas, S. Germanskiy, J.-C. Deinert, B. Green, I. Ilyakov, N. Awari, M. Chen, M. Bawatna, J. Ling, *et al.*, Non-perturbative terahertz high-harmonic generation in the three-dimensional Dirac semimetal Cd_3As_2, Nat. Commun. **11**, 2451 (2020).

[53] B. Cheng, N. Kanda, T. N. Ikeda, T. Matsuda, P. Xia, T. Schumann, S. Stemmer, J. Itatani, N. P. Armitage, and R. Matsunaga, Efficient terahertz harmonic generation with coherent acceleration of electrons in the Dirac semimetal Cd_3As_2, Phys. Rev. Lett. **124**, 117402 (2020).

[54] J. Lim, Y. S. Ang, F. J. García de Abajo, I. Kaminer, L. K. Ang, and L. J. Wong, Efficient generation of extreme terahertz harmonics in three-dimensional Dirac semimetals, Phys. Rev. Res. **2**, 043252 (2020).

[55] Y. Shao, S. Moon, A. N. Rudenko, J. Wang, J. Herzog-Arbeitman, M. Ozerov, D. Graf, Z. Sun, R. Queiroz, S. H. Lee, *et al.*, Semi-Dirac fermions in a topological metal, Phys. Rev. X **14**, 041057 (2024).

[56] J. Kim, S. S. Baik, S. H. Ryu, Y. Sohn, S. Park, B.-G. Park, J. Denlinger, Y. Yi, H. J. Choi, and K. S. Kim, Observation of tunable band gap and anisotropic Dirac semimetal state in black phosphorus, Science **349**, 723 (2015).

[57] X. Yuan, C. Zhang, Y. Liu, A. Narayan, C. Song, S. Shen, X. Sui, J. Xu, H. Yu, Z. An, *et al.*, Observation of quasi-two-dimensional Dirac fermions in $ZrTe_5$, NPG Asia Mater. **8**, e325 (2016).

[58] M. G. Olmos, Y. Baba, M. Amado, and R. A. Molina, Zero momentum topological insulator in 2D semi-Dirac materials, J. Phys.: Mater. **7**, 045008 (2024).

[59] N. Mohanta, J. M. Ok, J. Zhang, H. Miao, E. Dagotto, H. N. Lee, and S. Okamoto, Semi-Dirac and Weyl fermions in transition metal oxides, Phys. Rev. B **104**, 235121 (2021).

[60] S. Banerjee, R. R. P. Singh, V. Pardo, and W. E. Pickett, Tight-binding modeling and low-energy behavior of the semi-Dirac point, Phys. Rev. Lett. **103**, 016402 (2009).

[61] V. Pardo and W. E. Pickett, Half-metallic semi-Dirac-point generated by quantum confinement in TiO_2/VO_2 nanostructures, Phys. Rev. Lett. **102**, 166803 (2009).

[62] L. Medic, J. Mravlje, A. Ramšak, and T. Rejec, High-harmonic generation in semi-Dirac and Weyl semimetals with broken time-reversal symmetry: Exploration of the merging of Weyl nodes, Phys. Rev. B **109**, 205130 (2024).

[63] A. Bharti and G. Dixit, Role of topological charges in the nonlinear optical response from Weyl semimetals, Phys. Rev. B **107**, 224308 (2023).

[64] N. Rana, M. S. Mrudul, and G. Dixit, High-harmonic generation from strain-engineered graphene for polarization tailoring, Phys. Rev. B **110**, 054103 (2024).

[65] N. Rana, M. S. Mrudul, A. Bharti, S. Giri, and G. Dixit, Nonlinear optical spectroscopy of nodal line semimetals, Phys. Rev. Appl. **24**, L021001 (2025).

[66] M. S. Mrudul and G. Dixit, High-harmonic generation from monolayer and bilayer graphene, Phys. Rev. B **103**, 094308 (2021).

[67] D. Baykusheva, D. Zindel, V. Svoboda, E. Bommeli, M. Ochsner, A. Tehlar, and H. J. Wörner, Real-time probing of chirality during a chemical reaction, Proc. Natl. Acad. Sci. USA **116**, 23923 (2019).

[68] S. Giri, A. M. Dudzinski, J. C. Tremblay, and G. Dixit, Time-dependent electronic current densities in chiral molecules, Phys. Rev. A **102**, 063103 (2020).

[69] N. Rana and G. Dixit, Probing phonon-driven symmetry alterations in graphene via high-order-harmonic spectroscopy, Phys. Rev. A **106**, 053116 (2022).

[70] See Supplemental Material at http://link.aps.org/supplemental/10.1103/mxwy-m8zd for integrated harmonic yield as a function of the driving laser ellipticity and polarization sensitivity of the normalized harmonic yield for a driving wavelength of 2000 nm.

[71] S. Kandel, G. Gumbs, and O. L. Berman, Anisotropic optical conductivities of model topological nodal-line semimetals, J. Phys.: Condens. Matter **36**, 025301 (2024).

[72] G. Dixit, M. S. Mrudul and K. Prabhu, Data for high-harmonic generation from semi-Dirac materials [Dataset], Zenodo, 2026, https://doi.org/10.5281/zenodo.20079579.